Pentagraphite C_8: An all-sp^2 topological nodal-line semimetal

Jian-Tao Wang [1,2,3,*] Kun Bu,[1,2] Yuting Qian,[1,2] Hongming Weng [1,2,3,4] and Changfeng Chen[5]

[1]*Beijing National Laboratory for Condensed Matter Physics, Institute of Physics, Chinese Academy of Sciences, Beijing 100190, China*

[2]*School of Physical Sciences, University of Chinese Academy of Sciences, Beijing 100049, China*

[3]*Songshan Lake Materials Laboratory, Dongguan, Guangdong 523808, China*

[4]*CAS Center for Excellence in Topological Quantum Computation, University of Chinese Academy of Sciences, Beijing 100190, China*

[5]*Department of Physics and Astronomy, University of Nevada, Las Vegas, Nevada 89154, USA*

(Received 12 November 2021; accepted 17 December 2021; published 29 December 2021)

Recent research predicted stable two-dimensional pentagraphene in sp^2-sp^3 bonding states and three-dimensional pentadiamond (BC14) in all-sp^3 bonding states, both comprising five-membered carbon-ring networks and exhibiting semiconducting character with sizable electronic band gaps. Here we identify by *ab initio* calculations an all-sp^2 carbon allotrope, also comprising the unusual five-membered rings as the basic structural units, with an eight-atom monoclinic primitive cell in $C2/m$ (C_{2h}^3) symmetry, termed mpg-C_8 pentagraphite. Total-energy calculations show that mpg-C_8 is more stable than or comparable to the previously reported all-sp^2 rh6 polybenzene and all-sp^3 BC14 pentadiamond. Electronic band calculations reveal that mpg-C_8 is a topological nodal-line semimetal protected by the inversion (P) and time reversal (T) symmetry, comprising two nodal rings centered at the Γ and M points in the bulk first Brillouin zone and one projected surface flat band around the Fermi level on its (010) surface. These results establish a distinct type of carbon phase with nontrivial topological properties and offer insights into its outstanding electronic properties.

DOI: 10.1103/PhysRevB.104.245143

I. INTRODUCTION

Besides the well-known all-carbon structural phases of graphite and diamond, the past few decades have seen more than 500 carbon allotropes [1–31] that have been theoretically predicted or experimentally synthesized under laboratory conditions. Most notable among these carbon allotropes are carbon nanotubes [3], fullerenes [4], graphene [5], graphdiyne [12–14], and pentagraphene [28]. In addition, the supercubane (cub-C_8) carbon phase was theoretically predicted [32] and then synthesized from amorphous carbon films using a pulsed-laser induced liquid-solid interface reaction [33]; a rhombohedral crystalline modification of graphite (termed rh6 polybenzene) [34] in an all-sp^2 bonding network was suggested by *ab initio* calculations and confirmed experimentally in the milled fullerene soot [35]; and an all-sp^3 bonded full-fledged pentadiamond (BC14) [36] was reported to be present in carbon soot [37]. Two-dimensional (2D) pentagraphene in sp^2-sp^3 [28] bonding states and three-dimensional (3D) BC14 pentadiamond in all-sp^3 bonding networks [36], both comprising five-membered rings, have been predicted to be a semiconductor or insulator. Moreover, recent theoretical studies suggested that all-sp^2 or mixed sp^2-sp^3 carbon network structures [38–55] can be novel topological nodal-line semimetals (NLSMs).

Topological NLSMs are a fascinating class of quantum materials that possess extraordinary electronic and transport properties [56–69]. Generally, 3D allotropes of carbon formed by graphene networks can support two types of topological NLSM states [50]: type A that has closed nodal rings inside the first Brillouin zone (BZ) and type B that has nodal lines traversing the whole BZ. Nearly all-sp^2 hybridized allotropes tend to host the A-type closed nodal rings, such as Mackay-Terrones carbon crystal (MTC) [38], body-centered orthorhombic C_{16} (bco-C_{16}) [43], body-centered tetragonal C_{16} (bct-C_{16}) [44], and base-centered orthorhombic C_{16} (ors-C_{16}) [52], while the sp^2-sp^3 hybridized allotropes tend to host the B-type periodic nodal lines, such as interpenetrated graphene network C_6 (ign-C_6) [40], simple orthorhombic C_{12} (so-C_{12}) [45], and orthorhombic C_{24} (oC24) [46]. Furthermore, a monoclinic C_{24} (mrs-C_{24}) [53] was proposed to adopt an all-sp^2 hybridized network but holds the B-type paired nodal lines; meanwhile, an sp^2-sp^3 hybridized orthorhombic C_{16} (oP16) carbon allotrope [54] was reported to host two A-type closed nodal rings on the k_y=0 and π mirror planes. These topological nodal lines are protected by a combinational symmetry of spatial inversion (P) and time reversal (T) [38].

In this paper, we present by *ab initio* calculations a distinct type of carbon allotrope comprising five-membered rings in an all-sp^2 bonding network. This carbon structure has an eight-atom monoclinic primitive cell in $C2/m$ (C_{2h}^3) symmetry, thus termed mpg-C_8 pentagraphite. Its dynamic stability has been confirmed by phonon mode analysis. Total-energy calculations show that this structure is energetically more stable than or comparable to the previously reported all-sp^3 BC14 pentadiamond [36] and all-sp^2 rh6 polybenzene [34]. Electronic band calculations indicate that it is a topological NLSM protected by PT symmetry, comprising two nodal rings

*wjt@aphy.iphy.ac.cn

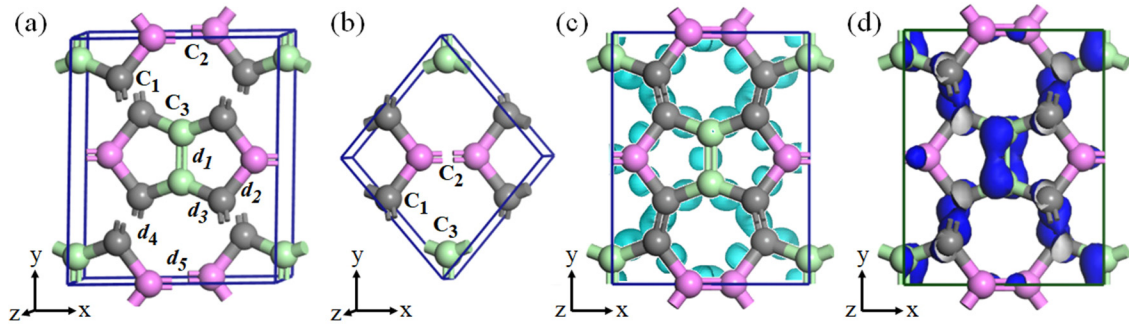

FIG. 1. (a) Crystalline structure of mpg-C_8 pentagraphite in $C2/m$ (C^3_{2h}, no. 12) symmetry. It has a 16-atom monoclinic unit cell constructed by two double-pentagonal rings with lattice parameters $a = 6.389$ Å, $b = 7.053$ Å, $c = 3.299$ Å, and $\beta = 119.65°$, occupying the 8j (0.7738, 0.1674, 0.1257), 4i (0.6122, 0.0, 0.0234), and 4h (0.0, 0.1, 0.5) Wyckoff positions denoted by C_1, C_2, and C_3, respectively. Here d_1, d_2, and d_3 indicate the bond lengths of the C_3=C_3 double bonds, C_1-C_2 and C_1-C_3 single bonds in the double-pentagonal rings; d_4 and d_5 indicate the double bond lengths of C_1=C_1 and C_2=C_2 between the double-pentagonal rings, respectively. (b) An eight-atom monoclinic primitive cell in $C2/m$ symmetry. (c) Electron localization function (ELF) map for mpg $-$ C_8 pentagraphite with an isosurface level of 0.75. (d) Partial charge density distribution of the topmost valence band with an isosurface level of 0.04 $e/$Å^3, mainly coming from the p_z orbitals of the C_1 and C_3 atoms. The structure in (c) and (d) is plotted along the z direction, which is topologically corresponding to the 2D carbon pentaheptite [79].

centered at the Γ and M points in the bulk first BZ. Meanwhile, when the nodal rings in the bulk are projected onto its (010) surface BZ, they produce one topologically protected surface flat band around the Fermi level. Moreover, simulated x-ray diffraction patterns of mpg-C_8 pentagraphite as well as rh6 polybenzene provide an excellent match to the previously unexplained distinct diffraction peaks found in carbon soot [70]. These results establish a distinct topological semimetal among carbon allotropes.

II. COMPUTATIONAL METHODS

Our calculations are carried out using the density functional theory as implemented in the Vienna *ab initio* simulation package (VASP) [71]. The generalized gradient approximation (GGA) developed by Armiento and Mattsson (AM05) [72] is adopted for the exchange-correlation potential. A plane-wave basis set with a large energy cutoff of 800 eV is used. The all-electron projector augmented wave (PAW) method [73] is adopted with $2s^22p^2$ treated as valence electrons. Convergence criteria employed for both the electronic self-consistent relaxation and the ionic relaxation are set to 10^{-8} eV and 0.01 eV/Å for energy and force, respectively. A hybrid density functional method based on the Heyd-Scuseria-Ernzerhof scheme (HSE06) [74] is used to calculate electronic band structures. Phonon calculations are performed using the PHONOPY package [75]. The topological invariant and surface states are calculated using the WANNIERTOOLS package [76] based on the maximally localized wannier functions (MLWFs) method with WANNIER90 [77,78].

III. RESULTS AND DISCUSSION

We first present structural characterization of the new mpg-C_8 carbon allotrope. As shown in Fig. 1(a), it has a 16-atom monoclinic unit cell comprising two double-pentagonal rings connected by ethene-type ($H_2C = CH_2$) π conjugation [2]. The lattice parameters are estimated to be $a = 6.389$ Å, $b = 7.053$ Å, $c = 3.299$ Å, and $\beta = 119.65°$, occupying the 8j (0.7738, 0.1674, 0.1257), 4i (0.6122, 0.0, 0.0234), and 4h (0.0, 0.1, 0.5) Wyckoff positions denoted by C_1, C_2, and C_3, respectively. There are three bond lengths 1.411 Å (d_1), 1.493 Å (d_2), and 1.440 Å (d_3) associated with C_3=C_3 double bonds and C_1-C_2 and C_1-C_3 single bonds in the double-pentagonal rings, and two distinct bond lengths 1.374 Å (d_4) and 1.364 Å (d_5) associated with C_1=C_1 and C_2=C_2 double bonds between the double-pentagonal rings, respectively. Also, there are three bond angles 104.54° for $\angle C_1$-C_2-C_1, 102.78° for $\angle C_2$-C_1-C_3, and 109.28° for $\angle C_1$-C_3=C_3 in the double-pentagonal rings; and three bond angles 141.45° for $\angle C_1$-C_3-C_1, 127.74° for $\angle C_1$-C_1-C_2, and 128.77° for $\angle C_1$-C_1-C_3 out of the double-pentagonal rings, respectively. These bond angles are averaged and equal to 119.09°, close to 120° in graphite with a large bond length range from 1.364 to 1.493 Å, similar to the bonds in all-sp^2 rh6 polybenzene [34] (see Table I). The primitive cell is given in Fig. 1(b). It has an eight-atom monoclinic primitive cell with lattice parameters $a = 4.759$ Å, $c = 3.297$ Å, $\alpha = 109.40°$, and $\gamma = 95.67°$. As shown in Figs. 1(c) and 1(d), this new 3D mpg-C_8 carbon structure is topologically corresponding to the planar carbon pentaheptite (consisting of pentagons and heptagons) [79] and can be derived from carbon pentaheptite with one C-C bond breaking in each heptagon, obeying the Wells approach [80].

To understand the bonding nature of electrons in mpg-C_8 carbon, we have calculated the electron localization function (ELF). The ELF maps can give a clear and quantitative description on the basic chemical bond (high ELF values $1 >$ ELF > 0.5 indicate the formation of covalent bonds) [81]. We plot the ELF map in Fig. 1(c) with an isosurface level of 0.75. It is seen that the electrons are well localized between the carbon-carbon bonds, showing a strong covalent bonding nature in this all-sp^2 mpg-C_8 carbon network structure.

Figure 2 shows the calculated total energy of mpg-C_8 carbon as a function of volume per atom in comparison with the results for the all-sp^2 rh6 polybenzene [34], bco-C_{16} [43],

TABLE I. Calculated equilibrium structural parameters (lattice parameters a, b, and c, volume per atom V_0, bond lengths d_{C-C}), total energy per atom E_{tot}, bulk modulus B_0, and electronic band gap E_g for graphite, diamond, BC14, cub-C_8, rh6, bco-C_{16}, ors-C_{16}, mrs-C_{24}, and mpg-C_8 pentagraphite, compared to the reported data [29,34,36,37,43,52,53,83].

Structure	Space group	Method	a (Å)	b (Å)	c (Å)	V_0 (Å^3)	d_{C-C} (Å)	E_{tot} (eV)	B_0 (GPa)	E_g (eV)
Diamond	$Fd\bar{3}m$	AM05	3.552			5.60	1.538	−9.018	451	5.36
		EXP [83]	3.567			5.67	1.544		446	5.47
BC14	$I2_13$	AM05 [36]	5.545			6.09	1.498–1.824	−8.517	386	5.64
		EXP [37]	5.545							
cub-C_8	$Im\bar{3}m$	AM05 [29]	4.853			7.15	1.470, 1.578	−8.355	323	4.17
rh6	$R\bar{3}m$	AM05 [34]	6.902	3.470		7.96	1.359, 1.483	−8.550	291	0.47
bco-C_{16}	$Imma$	AM05 [43]	7.806	4.877	3.237	7.70	1.382–1.459	−8.671	315	NLSM
ors-C_{16}	$Cccm$	AM05 [52]	3.318	8.372	4.915	8.02	1.421–1.438	−8.810	298	NLSM
mrs-C_{24}	$P2/m$	AM05 [53]	4.921	3.421	12.611	8.30	1.417–1.441	−8.882	290	NLSM
mpg-C_8	$C2/m$	AM05	6.389	7.053	3.299	8.07	1.364–1.493	−8.568	285	NLSM
Graphite	$P6_3/mmc$	AM05	2.462	6.710		8.81	1.422	−9.045	280	
		EXP [83]	2.460	6.704		8.78	1.420		286	

ors-C_{16} [52], mrs-C_{24} [53], all-sp^3 cub-C_8 cubane [29], all-sp^3 BC14 pentadiamond [36], diamond, and graphite. The results show that mpg-C_8 carbon is energetically less stable than bco-C_{16}, ors-C_{16}, mrs-C_{24}, diamond, and graphite, but more stable than the reported cub-C_8 supercubane, BC14 pentadiamond, rh6 polybenzene, and 2D pentagraphene [28], suggesting its good energetic stability. The calculated equilibrium volume is 8.07 Å^3/atom for mpg-C_8, which is larger than 6.09 Å^3/atom for BC14, 7.15 Å^3/atom for cub-C_8, 7.70 Å^3/atom for bco-C_{16}, and close to 7.96 Å^3/atom for rh6, 8.02 Å^3/atom for ors-C_{16}, while smaller than 8.30 Å^3/atom for mrs-C_{24} carbon. From the Murnaghan fit [82] of the total energy curves, the bulk modulus (B_0) of mpg-C_8 carbon is estimated to be 285 GPa, which is smaller than the value in all-sp^3 bonded diamond, C_8 cubane, and BC14 pentadiamond, but closer to the value of 291 GPa for rh6 and 280 GPa for graphite in all-sp^2 bonding, showing typical characters of an all-sp^2 bonding carbon structure. The calculated equilibrium structural parameters, total energy, band gaps, and bulk modulus values for these carbon allotropes are listed in Table I, compared with available experimental data [37,83].

To confirm the dynamical stability of mpg-C_8 carbon, we have calculated its phonon band spectrum and partial density of states (PDOS). As shown in Fig. 3, the highest phonon frequency is about 1616 cm^{-1} at the Z point. Meanwhile, the PDOS results indicate that the highest phonon bands around 1600 cm^{-1} correspond to the C_1=C_1 and C_3=C_3 double bonds and the peaks around 1400 cm^{-1} mainly correspond to the C_2=C_2 double bonds. Below 1000 cm^{-1}, the phonon spectrum comprises a mixing of contributions from the single bonds of C_1, C_2, and C_3 atoms. No imaginary frequencies exist in the entire BZ, confirming the dynamic stability of the predicted mpg-C_8 pentagraphite.

To examine the thermal stability of mpg-C_8 carbon, we have also performed *ab initio* molecular dynamics simulations in the canonical (*NVT*) ensemble with the Nosé

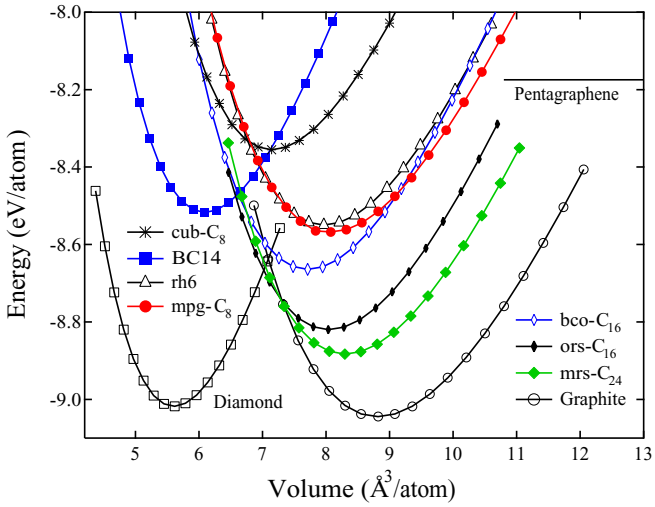

FIG. 2. Total energy as a function of volume per atom for mpg-C_8 pentagraphite in comparison with diamond, graphite, rh6 polybenzene [34], bco-C_{16} [43], ors-C_{16} [52], mrs $-$ C_{24} [53], cub $-$ C_8 cubane [29], and BC14 pentadiamond [36]. The energy for 2D pentagraphene [28] is also shown for comparison.

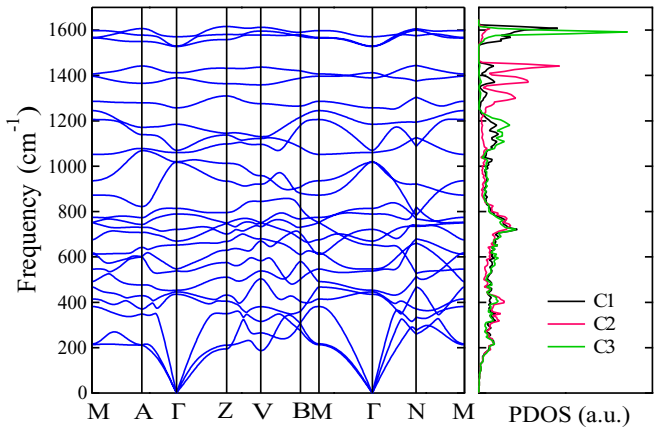

FIG. 3. Phonon band structures and PDOS for mpg-C_8 carbon at equilibrium lattice parameters. The full BZ and high symmetric points are defined in Fig. 4(b). No imaginary frequencies exist throughout the entire BZ, confirming the dynamic stability of mpg-C_8 carbon.

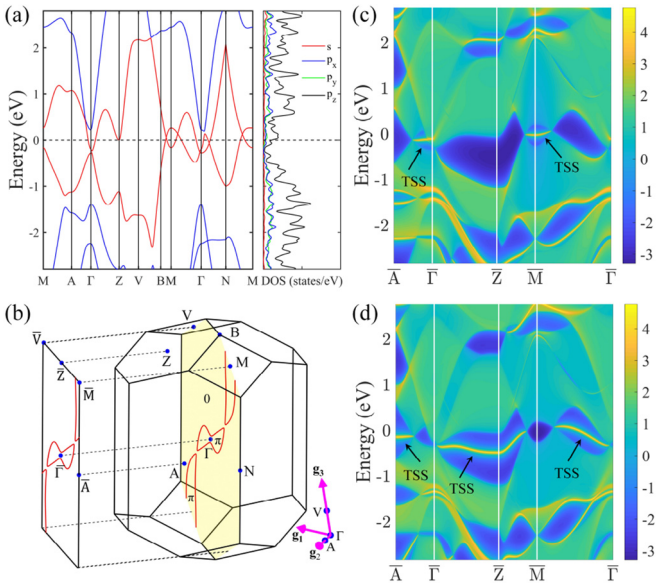

FIG. 4. Calculated bulk and surface band structures of mpg-C_8 carbon at equilibrium lattice parameters. The Fermi level is set to zero. (a) The bulk band structure along the M (−0.5, 0.5, 0.5), A (0.0, 0.5, 0.0), Γ (0.0, 0.0, 0.0), Z (0.0, 0.5, 0.5), V (0.0, 0.0, 0.5), B (−0.406, 0.406, 0.606), M (−0.5, 0.5, 0.5), Γ (0.0, 0.0, 0.0), N (−0.406, 0.406, 0.0), and M (−0.5, 0.5, 0.5) high symmetric k points. The bands near the Fermi level marked in red cross along the B-M, M-Γ, Γ − N and N-M directions. The projected density of states (DOSs) are also given in (a). (b) The first BZ and high-symmetry points, along with two nodal rings centered at the Γ and M points in the shaded mirror plane. The projected (010) surface BZ $\bar{V}$-$\bar{Z}$-$\bar{M}$-$\bar{A}$-$\bar{\Gamma}$ (left) is shown relative to the high symmetric V-Z-M-A-Γ directions in the bulk BZ, parallel to the $k_y = 0$ mirror plane. Shown in (c) and (d) are the topological surface states (TSSs) with beard type (c) and zigzag type (d) terminations of the (010) surface. The surface flat band can be inside (c) or outside (d) the surface projected nodal rings.

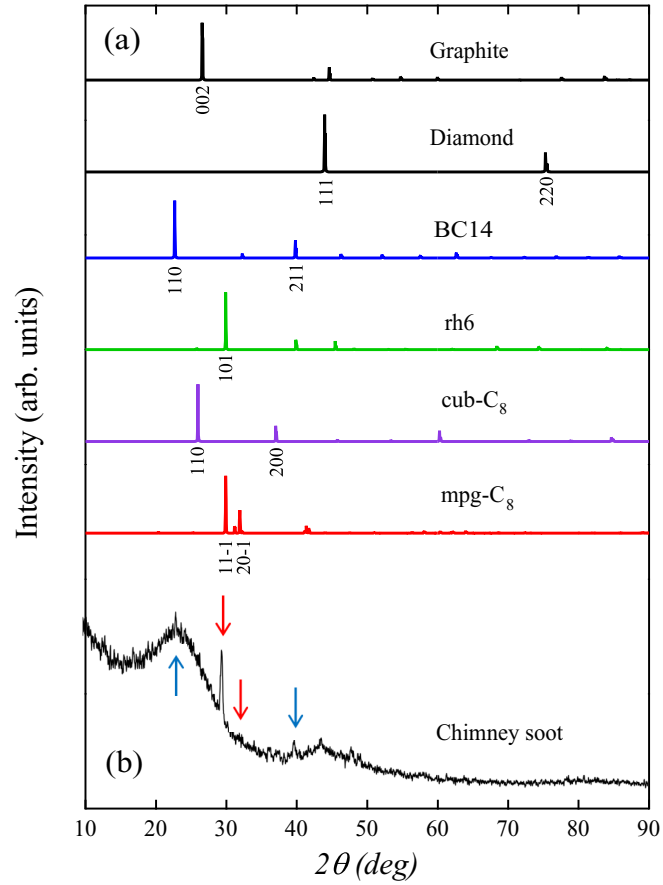

FIG. 5. (a) Simulated XRD patterns for graphite, diamond, BC14, rh6, cub-C_8, and mpg-C_8 pentagraphite. (b) Experimental XRD patterns for the chimney soot [70]. The x-ray wavelength is 1.5406 Å with a copper source. The red and blue arrows indicate the relative patterns for mpg-C_8 pentagraphite and BC14 pentadiamond, respectively.

thermostat [84]. The energy fluctuations at 300 and 1200 K with the structures after 5 ps simulation are presented in Fig. S1 in the Supplemental Material [85]. After heating up to 1200 K for 5 ps, no structural changes occur. Some carbon atoms deviate from the equilibrium positions appreciably, but they can be relaxed back to the beginning optimized structures. Combining the phonon and AIMD simulations, it can be concluded that mpg-C_8 has robust stability at room temperature.

We next discuss the electronic properties of mpg-C_8 carbon. Figure 4(a) shows the calculated band structures and projected density of states (DOSs) without considering the spin-orbit coupling (SOC), and it is seen that the bands near the Fermi level (E_F) cross along the high-symmetric B-M, M-Γ, Γ-N, and N-M directions. A detailed analysis of the nodal points in three dimensions shows that there are two nodal rings centered at the high-symmetric Γ and M points inside the first BZ and constrained in the $k_y = 0$ mirror plane [shaded with yellow in Fig. 4(b), including high-symmetric V, B, M, N, and Γ points]. The two nodal rings are enforced due to the band inversion mechanism and protected by PT and mirror symmetry. For an inversion symmetric system without SOC, the symmetry-based indicators [86–88] $\mathbb{Z}_{2,2,2,4} = (z_{2,1}, z_{2,2}, z_{2,3}, z_{2,4})$ are utilized to indicate a nontrivial topological classification. In the present case, by counting the parity eigenvalues at the maximal high-symmetric $\boldsymbol{k}$ points, the symmetry-based indicator for mpg-C_8 carbon is calculated to be (1,1,1,0), which indicates that the $k_i = 0$ or $k_i = \pi$ ($i = 1, 2, 3$) should be crossed by nodal lines for 2 mod 4 times [88], thus the two nodal rings in $k_y = 0$ plane for mpg-C_8 carbon can be understood from the symmetry-based indicator theory. When SOC is considered, it is easy to check that mpg-C_8 carbon is a weak topological insulator with $\mathbb{Z}_2$ index as (0;1,1,1). Meanwhile, the projected DOSs [see Fig. 4(a)] and band-decomposed partial charge density distribution [see Fig. 1(d)] show that the states near E_F are mainly coming from the p_z orbitals of the C_1 and C_3 atoms.

To understand the orbital contributions of the nodal lines, we have performed an orbital character analysis by plotting the fat band structures of mpg-C_8 carbon for carbon p_x, p_y, and p_z orbitals [see Figs. S2(a)–S2(c) in the Supplemental Material [85]]. It is clearly seen that the band structures around the E_F are mainly contributed by the carbon p_z orbitals, which is consistent with the DOS calculations shown in Fig. 4(a). To further explore the topological electronic properties of mpg-C_8 carbon, we have constructed an eight-band TB

model based on the carbon p_z orbitals with MLWFs method [77,78]. Then based on the established TB model, we have simulated the (010) surface band structures using an iterative Green's function method [76]. When the surface termination is a beard type [89], the drumheadlike surface states can be seen inside the projected $\overline{\Gamma}$ and $\overline{M}$ centered nodal rings [see Fig. 4(c)]; when the surface termination is a zigzag type, the drumheadlike surface states can be outside the projected $\overline{\Gamma}$ and $\overline{M}$ centered nodal rings [see Fig. 4(d)]. To confirm the topological origin of the surface states, we have calculated the Berry phases accumulated along three lines across the entire BZ: two lines going through the two nodal rings separately and another line outside the two rings [see Fig. 4(b)]. The Berry phases are calculated to be π inside and 0 outside the two nodal rings as indicated in Fig. 4(b), which gives a topological classification, thus the topological nontrivial drumheadlike surface states can be expected inside or outside the two topological nodal rings.

Finally, to establish experimental connection of mpg-C_8 carbon, we have simulated its x-ray diffraction (XRD) spectra along with those for graphite, diamond, rh6, cub-C_8, and BC14 pentadiamond [see Fig. 5(a)], and compared the results with experimental XRD data of carbon soot [70]. As shown in Fig. 5(b), the measured XRD spectra reveal a considerable amount of amorphous carbon and provide clear evidence for several crystalline phases in the recovered specimen. The prominent peak around 43.7°, matching that of the diamond (111) diffraction, the main peak at 23° and small peak at 40°, matching that of BC14 (110) and (211) XRD spectra; meanwhile, the most distinct feature of the measured XRD spectra is a strong peak near 30°, which is attributed to the rh6 (101) diffraction [34] and also match well with the $(11\bar{1})$ main peak for mpg-C_8 carbon. These results suggest that mpg-C_8 carbon is a possible candidate of the new carbon phase observed in the chimney carbon soot [70].

IV. SUMMARY

In summary, we have identified by means of *ab initio* calculations a distinct type of monoclinic carbon allotrope constructed by pentagonal rings in $C2/m$ symmetry. This all-sp^2 hybridized mpg-C_8 pentagraphite is energetically more stable than or comparable to the previously reported all-sp^2 rh6 polybenzene [34] and all-sp^3 BC14 pentadiamond [36]. Electronic band calculations indicate that mpg-C_8 is a topological nodal-line semimetal protected by inversion (P) and time reversal (T) symmetry, comprising two nodal rings centered at the Γ and M points in the bulk first Brillouin zone and one projected surface flat band around the Fermi level on its (010) surface. Moreover, simulated x-ray diffraction patterns of mpg-C_8 pentagraphite provide a good match to distinct diffraction peaks found in carbon soot [70]. These findings expand the realm of nodal manifolds in topological semimetals and improve our understanding on the structural and electronic properties of 3D carbon network structures with pentagon units [90–92].

ACKNOWLEDGMENTS

This study was supported by the National Natural Science Foundation of China (Grants No. 11674364, No. 11674369, No. 11974387, No. 11925408, No. 11921004, and No. 12188101), the Strategic Priority Research Program of the Chinese Academy of Sciences (Grants No. XDB33000000 and No. XXH13506-202), and the National Key Research and Development Program of China (Grants No. 2018YFA0305700 and No. 2020YFA0711502). H.W. acknowledges support from the K. C. Wong Education Foundation (Grant No. GJTD-2018-01), the Beijing Natural Science Foundation (Grant No. Z180008), and the Beijing Municipal Science and Technology Commission (Grant No. Z191100007219013).

[1] E. A. Belenkov and V. A. Greshnyakov, Phys. Solid State **55**, 1754 (2013).
[2] J. T. Wang, C. F. Chen, and Y. Kawazoe, Sci. Rep. **3**, 03077 (2013).
[3] S. Iijima, Nature (London) **354**, 56 (1991).
[4] H. W. Kroto, J. R. Heath, S. C. O'brien, R. F. Curl, and R. E. Smalley, Nature (London) **318**, 162 (1985).
[5] K. S. Novoselov, A. K. Geim, S. V. Morozov, D. Jiang, Y. Zhang, S. V. Dubonos, I. V. Grigorieva, and A. A. Firsov, Science **306**, 666 (2004).
[6] M. O'Keeffe, G. B. Adams, and O. F. Sankey, Phys. Rev. Lett. **68**, 2325 (1992).
[7] W. A. Chalifoux and R. R. Tykwinski, Nat. Chem. **2**, 967 (2010).
[8] H. R. Karfunkel and T. Dresslert, J. Am. Chem. Soc. **114**, 2285 (1992).
[9] Q. Li, Y. M. Ma, A. R. Oganov, H. B. Wang, H. Wang, Y. Xu, T. Cui, H. K. Mao, and G. T. Zou, Phys. Rev. Lett. **102**, 175506 (2009).
[10] K. Umemoto, R. M. Wentzcovitch, S. Saito, and T. Miyake, Phys. Rev. Lett. **104**, 125504 (2010).
[11] X. L. Sheng, Q. B. Yan, F. Ye, Q. R. Zheng, and G. Su, Phys. Rev. Lett. **106**, 155703 (2011).
[12] R. H. Baughman, H. Eckhardt, and M. Kertesz, J. Chem. Phys. **87**, 6687 (1987).
[13] M. M. Haley, S. C. Brand, and J. J. Pak, Angew. Chem. Int. Ed. Engl. **36**, 836 (1997).
[14] G. Li, Y. Li, H. Liu, Y. Guo, and D. Zhu, Chem. Commun. **46**, 3256 (2010).
[15] J. T. Wang, C. F. Chen, and Y. Kawazoe, Phys. Rev. Lett. **106**, 075501 (2011).
[16] H. Y. Niu, X. Q. Chen, S. B. Wang, D. Z. Li, W. L. Mao, and Y. Y. Li, Phys. Rev. Lett. **108**, 135501 (2012).
[17] M. Amsler, J. A. Flores-Livas, L. Lehtovaara, F. Balima, S. A. Ghasemi, D. Machon, S. Pailhès, A. Willand, D. Caliste, S. Botti, A. San Miguel, S. Goedecker, and M. A. L. Marques, Phys. Rev. Lett. **108**, 065501 (2012).
[18] Z. S. Zhao, B. Xu, X. F. Zhou, L. M. Wang, B. Wen, J. L. He, Z. Y. Liu, H. T. Wang, and Y. J. Tian, Phys. Rev. Lett. **107**, 215502 (2011).
[19] Z. S. Zhao, F. Tian, X. Dong, Q. Li, Q. Q. Wang, H. Wang, X. Zhong, B. Xu, D. L. Yu, J. L. He, H. T. Wang,

Y. M. Ma, and Y. J. Tian, J. Am. Chem. Soc. **134**, 12362 (2012).
[20] J. T. Wang, C. F. Chen, and Y. Kawazoe, Phys. Rev. B **85**, 033410 (2012).
[21] C. X. Zhao, C. Y. Niu, Z. J. Qin, X. Y. Ren, J. T. Wang, J. H. Cho, and Y. Jia, Sci. Rep. **6**, 21879 (2016).
[22] Z. Z. Li, J. T. Wang, L. F. Xu, and C. F. Chen, Phys. Rev. B **94**, 174102 (2016).
[23] K. Bu, Z. Z. Li, and J. T. Wang, J. Chem. Phys. **147**, 064512 (2017).
[24] J. T. Wang, C. F. Chen, H. D. Li, H. Mizuseki, and Y. Kawazoe, Sci. Rep. **6**, 24665 (2016).
[25] M. Hu, F. Tian, Z. S. Zhao, Q. Huang, B. Xu, L. M. Wang, H. T. Wang, Y. J. Tian, and J. L. He, J. Phys. Chem. C **116**, 24233 (2012).
[26] Z. Z. Li, C. S. Lian, J. Xu, L. F. Xu, J. T. Wang, and C. F. Chen, Phys. Rev. B **91**, 214106 (2015).
[27] D. Selli, I. A. Baburin, R. Martoňák, and S. Leoni, Phys. Rev. B **84**, 161411(R) (2011).
[28] S. H. Zhang, J. Zhou, Q. Wang, X. S. Chen, Y. Kawazoe, and P. Jena, Proc. Natl. Acad. Sci. USA **112**, 2372 (2015).
[29] J. T. Wang, C. F. Chen, H. Mizuseki, and Y. Kawazoe, Phys. Chem. Chem. Phys. **20**, 7962 (2018).
[30] R. Hoffmann, A. A. Kabanov, A. A. Golov, and D. M. Proserpio, Samara Carbon Allotrope Database, http://sacada.sctms.ru.
[31] P. Avery, X. Wang, C. Oses, E. Gossett, D. M. Proserpio, C. Toher, S. Curtarolo, and E. Zurek, npj Comput. Mater. **5**, 89 (2019).
[32] J. K. Burdett and S. Lee, J. Am. Chem. Soc. **107**, 3063 (1985).
[33] P. Liu, H. Cui, and G. W. Yang, Cryst. Growth Des. **8**, 581 (2008).
[34] J. T. Wang, C. F. Chen, E. G. Wang, and Y. Kawazoe, Sci. Rep. **4**, 04339 (2014).
[35] H. A. Calderon, I. Estrada-Guel, F. Alvarez-Ramírez, V. G. Hadjiev, and F. C. Robles Hernandez, Carbon **102**, 288 (2016).
[36] J. T. Wang, C. F. Chen, and H. Mizuseki, Phys. Rev. B **102**, 184106 (2020).
[37] R. B. Aust and H. G. Drickamer, Science **140**, 817 (1963).
[38] H. Weng, Y. Liang, Q. Xu, R. Yu, Z. Fang, X. Dai, and Y. Kawazoe, Phys. Rev. B **92**, 045108 (2015).
[39] K. Mullen, B. Uchoa, and D. T. Glatzhofer, Phys. Rev. Lett. **115**, 026403 (2015).
[40] Y. Chen, Y. Xie, S. A. Yang, H. Pan, F. Zhang, M. L. Cohen, and S. B. Zhang, Nano Lett. **15**, 6974 (2015).
[41] X. Dong, M. Hu, J. L. He, Y. J. Tian, and H. T. Wang, Sci. Rep. **5**, 10713 (2015).
[42] Y. Cheng, J. Du, R. Melnik, Y. Kawazoe, and B. Wen, Carbon **98**, 468 (2016).
[43] J. T. Wang, H. Weng, S. Nie, Z. Fang, Y. Kawazoe, and C. F. Chen, Phys. Rev. Lett. **116**, 195501 (2016).
[44] Y. Cheng, X. Feng, X. T. Cao, B. Wen, Q. Wang, Y. Kawazoe, and P. Jena, Small **13**, 1602894 (2017).
[45] J. T. Wang, C. F. Chen, and Y. Kawazoe, Phys. Rev. B **97**, 245147 (2018).
[46] Z. Z. Li, J. Chen, S. Nie, L. F. Xu, H. Mizuseki, H. Weng, and J. T. Wang, Carbon **133**, 39 (2018).
[47] X. Feng, Q. S. Wu, Y. Cheng, B. Wen, Q. Wang, Y. Kawazoe, and P. Jena, Carbon **127**, 527 (2018).
[48] J. T. Wang, S. Nie, H. Weng, Y. Kawazoe, and C. F. Chen, Phys. Rev. Lett. **120**, 026402 (2018).
[49] Y. Gao, Y. Chen, Y. Xie, P. Y. Chang, M. L. Cohen, and S. Zhang, Phys. Rev. B **97**, 121108(R) (2018).
[50] J. T. Wang, H. Weng, and C. F. Chen, Adv. Phys. X **4**, 1625724 (2019).
[51] J. T. Wang, Y. Qian, H. Weng, E. G. Wang, and C. F. Chen, J. Phys. Chem. Lett. **10**, 2515 (2019).
[52] Z. Zhao, Y. Hang, Z. Zhang, and W. Guo, Phys. Rev. B **100**, 115420 (2019).
[53] Z. Zhao, Z. Zhang, and W. Guo, J. Mater. Chem. C **8**, 1548 (2020).
[54] K. Bu, J. T. Wang, H. Weng, and C. F. Chen, Phys. Rev. B **101**, 205104 (2020).
[55] K. Bu, Y. Qian, J. T. Wang, and H. Weng, Phys. Rev. B **103**, L081108 (2021).
[56] A. A. Burkov, M. D. Hook, and L. Balents, Phys. Rev. B **84**, 235126 (2011).
[57] M. Phillips and V. Aji, Phys. Rev. B **90**, 115111 (2014).
[58] C. Fang, Y. Chen, H. Y. Kee, and L. Fu, Phys. Rev. B **92**, 081201(R) (2015).
[59] R. Yu, H. Weng, Z. Fang, X. Dai, and X. Hu, Phys. Rev. Lett. **115**, 036807 (2015).
[60] T. T. Heikklia and G. E. Volovik, New J. Phys. **17**, 093019 (2015).
[61] L. S. Xie, L. M. Schoop, E. M. Seibel, Q. D. Gibson, W. Xie, and R. J. Cava, APL Mater. **3**, 083602 (2015).
[62] Y. H. Chan, C. K. Chiu, M. Y. Chou, and A. P. Schnyder, Phys. Rev. B **93**, 205132 (2016).
[63] T. Bzdusek, Q. S. Wu, A. Ruegg, M. Sigrist, and A. A. Soluyanov, Nature (London) **538**, 75 (2016).
[64] Z. Yan and Z. Wang, Phys. Rev. Lett. **117**, 087402 (2016).
[65] G. E. Volovik, Phys. Scr. **T164**, 014014 (2015).
[66] Q. Xu, R. Yu, Z. Fang, X. Dai, and H. Weng, Phys. Rev. B **95**, 045136 (2017).
[67] C. Fang, H. Weng, X. Dai, and Z. Fang, Chin. Phys. B **25**, 117106 (2016).
[68] Y. Kim, B. J. Wieder, C. L. Kane, and A. M. Rappe, Phys. Rev. Lett. **115**, 036806 (2015).
[69] T. Hyart, R. Ojajärvi, and T. T. Heikkilä, J. Low Temp. Phys **191**, 35 (2018).
[70] D. Pantea, S. Brochu, S. Thiboutot, G. Ampleman, and G. Scholz, Chemosphere **65**, 821 (2006).
[71] G. Kresse and J. Furthmüller, Phys. Rev. B **54**, 11169 (1996).
[72] R. Armiento and A. E. Mattsson, Phys. Rev. B **72**, 085108 (2005).
[73] P. E. Blöchl, Phys. Rev. B **50**, 17953 (1994).
[74] A. V. Krukau, O. A. Vydrov, A. F. Izmaylov, and G. E. Scuseria, J. Chem. Phys. **125**, 224106 (2006).
[75] A. Togo, F. Oba, and I. Tanaka, Phys. Rev. B **78**, 134106 (2008).
[76] Q. S. Wu, S. N. Zhang, H. F. Song, M. Troyer, and A. A. Soluyanov, Comput. Phys. Commun. **224**, 405 (2018).
[77] A. A. Mostofi, J. R. Yates, Y. S. Lee, I. Souza, D. Vanderbilt, and N. Marzari, Comput. Phys. Commun. **178**, 685 (2008).
[78] N. Marzari, A. A. Mostofi, J. R. Yates, I. Souza, and D. Vanderbilt, Rev. Mod. Phys. **84**, 1419 (2012).
[79] V. H. Crespi, L. X. Benedict, M. L. Cohen, and S. G. Louie, Phys. Rev. B **53**, R13303 (1996).
[80] A. F. Wells, Acta Crystallogr. **7**, 535 (1954).
[81] B. Silvi B and A. Savin, Nature (London) **371**, 683 (1994).

[82] F. D. Murnaghan, Proc. Natl. Acad. Sci. U.S.A. **30**, 244 (1944).
[83] F. Occelli, P. Loubeyre, and R. Letoullec, Nat. Mater. **2**, 151 (2003).
[84] S. Nosé, J. Chem. Phys. **81**, 511 (1984).
[85] See Supplemental Material at http://link.aps.org/supplemental/10.1103/PhysRevB.104.245143 for the thermal stability (Fig. S1) and fat band structures (Fig. S2), which includes Ref. [84].
[86] H. C. Po, A. Vishwanath, and H. Watanabe, Nat. Commun. **8**, 50 (2017).
[87] Z. Song, T. Zhang, Z. Fang, and C. Fang, Nat. Commun. **9**, 3530 (2019).
[88] Z. Song, T. Zhang, and C. Fang, Phys. Rev. X **8**, 031069 (2018).
[89] S. Ryu and Y. Hatsugai, Phys. Rev. Lett. **89**, 077002 (2002).
[90] D. Y. Ni, Y. H. Shen, Y. P. Shen, Q. Wang, Y. Kawazoe, and P. Jena, Carbon **183**, 652 (2021).
[91] S. Y. Li, Y. H. Shen, D. Y. Ni, and Q. Wang, J. Mater. Chem. A **9**, 23214 (2021).
[92] D. Ni, Y. Guo, Y. Shen, and Q. Wang, Adv. Theory Simul. **4**, 2100025 (2021).